SPH/N-body simulations of small (D = 10 km) asteroidal breakups and improved parametric relations for Monte–Carlo collisional models

M. Brož, P. Ševeček or vice versa

Institute of Astronomy, Charles University, Prague, V Holešovičkách 2, 18000 Prague 8, Czech Republic e-mail: mira@sirrah.troja.mff.cuni.cz

D. Nesvorný, B. Enke, D. Durda, E. Asphaug, K. Walsh, D. Richardson

Abstract

We report on our study of asteroidal breakups, i.e. fragmentations of targets, subsequent gravitational reaccumulation and formation of small asteroid families. We focused on parent bodies with diameters $D_{\rm pb}$ = 10 km. Simulations were performed with a smoothed-particle hydrodynamics (SPH) code combined with an efficient N-body integrator. We assumed various projectile sizes, impact velocities and impact angles (125 runs in total). Resulting size-frequency distributions are significantly different from scaled-down simulations with $D_{\rm pb}$ = 100 km targets (Durda et al., 2007). We derive new parametric relations describing fragment distributions, suitable for Monte-Carlo collisional models. We also characterize velocity fields and angular distributions of fragments, which can be used in N-body simulations of small asteroid families. Finally, we discuss a number of uncertainties related to SPH simulations.

...

Keywords: Asteroids, dynamics, Collisional physics, Impact processes

1. Introduction and motivation

Collisions between asteroids play an important role in the evolution of the main belt. Understanding the fragmentation process and subsequent reaccumulation of fragments is crucial for studies of the formation of the solar system or the internal structure of the asteroids. Remnants of past break-ups are preserved to a certain extent in the form of asteroid families – groups of asteroids located close to each other in the space of proper elements $a_{\rm p}$, $e_{\rm p}$, $I_{\rm p}$ (Hirayama, 1918; Nesvorný et al., 2015).

The observed size-frequency distribution (SFD) of the family members contains a lot of information and can aid us to determine the mass $M_{\rm PB}$ of the parent body. However, it cannot be determined by merely summing up the observed family members, as a large portion of the total mass is presumably 'hidden' in fragments well under observational completeness. The SFD is also modified over time, due to ongoing secondary collisional evolution, a dynamical removal by the Yarkovsky drift and various gravitational resonances, etc. This makes the procedure a bit difficult for ancient asteroid families and relatively simple for very young ($<$ 10 Myr) clusters, such as Karin or Veritas (Nesvorný et al., 2006; Michel et al., 2011).

The collisions has been studied experimentally, using impacts into cement mortar targets (Davis and Ryan, 1990; Nakamura and Fujiwara, 1991). However, in order to compare those results to impacts of asteroids we need to scale the results up in terms of the mass of the target and kinetic energy of the projectile by several orders of magnitude. The scaled impact experiments can still have significantly different outcomes, compared to the asteroid collisions, due to increasing role of gravitational compression, different fragmentation mechanisms etc. Experiments yield valuable information about properties of materials, but they are not sufficient to unambiguously determine results of asteroid collisions.

Numerical simulations are thus used to solve a standard set of hydrodynamic equations; however, the physics of fragmentation is much more complex than that. Especially for low-energy cratering impacts, it is necessary to simulate an explicit propagation of cracks in the target. There is no *ab initio* theory of fragmentation, but phenomenological theories has been developed to describe the fragmentation process, such as the Grady–Kipp model of fragmentation (Grady and Kipp, 1980), used in this paper, or more complex models including porosity based on P-α model (Herrmann, 1969).

Common methods of choice for studying impacts are shock-physics codes and particle codes (Jutzi et al., 2015). The most important outputs of simulations are masses $M_{\rm lr}$ and $M_{\rm lf}$ of the largest remnant and largest fragment, respectively, and the exponent q of the power-law approximation to the cumulative size-frequency distribution $N(>D)$, i. e. the number N of family members with diameter larger than given D. Parametric relations, describing the dependence of $M_{\rm lr}$ and q on input parameters, can be then applied on collisional models of the main asteroid belt, such as the one in Morbidelli et al. (2009) or Cibulková et al. (2014); however, if we aim to determine the size of the parent body, we need to solve an *inverse* problem.

A single simulation gives us the SFD for a given size of the parent body and several parameters of the impactor. However, if one wishes to derive the size of the parent body and impactor parameters from the observed SFD, it is necessary to conduct a

large set of simulations with different parameters and then find the SFD that resembles the observed one as accurately as possible. This makes the problem difficult as the parameter space is quite extensive. For one run, we usually have to specify the parent body size $D_{\rm PB}$, the projectile size $d_{\rm project}$, the impact velocity $v_{\rm imp}$, and the impact angle $\phi_{\rm imp}$ (i.e. the angle between the velocity vector of the impactor and the inward normal of the target at the point of collision). Other parameters of the problem are the material properties of considered asteroids, such as bulk density, shear modulus, porosity etc.

Due to the extent of the parameter space, a thorough study would be highly demanding on computational resources. It is therefore reasonable to fix the size of the parent body and study breakups with various parameters of the impactor.

A large set of simulations was published by Durda et al. (2007), who studied disruptions of 100 km monolithic targets. Similarly, Benavidez et al. (2012) performed an analogous set of simulations with rubble-pile targets. They also used the resulting SFDs to estimate the size of the parent body for a number of asteroid families. As the diameter of the parent body is never exactly 100 km, the computed SFDs have to be multiplied by a suitable scaling factor $f_{\rm scale}$ to match the observed one. However, small families have been already discovered (e.g. Datura, Nesvorný et al. (2015)) and their parent-body size is likely $D_{\rm pb} = 10$ km, i.e. an order-of-magnitude smaller. The linearity of the scaling is a crucial assumption and we will assess the plausibility of this assumption in this paper.

To fill up a gap in the parameter space, we proceed with small targets. We carried out a set of simulations with $D_{\rm pb} = 10$ km parent bodies and carefully compared them with the simulations of Durda et al. (2007).

The paper is organised as follows. In Section 2, we briefly describe our numerical methods. The results of simulations are presented in Section 3. Using the computed SFDs we derive parametric relations for the slope q and the masses $M_{\rm lr}$ and $M_{\rm lf}$ of the largest remnant and the largest fragment, respectively, in Section 4. Finally, we summarize our work in Section 5.

2. Numerical methods

We follow a hybrid approach of Michel et al. (2001, 2002, 2003, 2004), employing an SPH discretization for the simulation of fragmentation and an N-body integrator for subsequent gravitational reaccumulation. Each simulation can be thus divided to three phases: i) a fragmentation, ii) a hand-off, and iii) a reaccumulation. We shall describe them sequentially in the following subsections.

2.1. Fragmentation phase

The first phase of the collision is described by hydrodynamical equations in a lagrangian frame. They properly account for supersonic shock wave propagation and fragmentation of the material. We use `SPH5` code by Benz and Asphaug (1994) for their numerical solution. In the following, we present only a brief description of equations used in our simulations and we refer a reader to extensive reviews of the method (Rosswog, 2009; Cossins, 2010; Price, 2008, 2012) for more detailed description.

Our problem is specified by four basic equations, namely the equation of continuity, equation of motion, energy equation and Hooke's law:

$$\frac{\mathrm{d}\rho}{\mathrm{d}t} = -\rho\nabla\cdot\boldsymbol{v}\,, \tag{1}$$

$$\frac{\mathrm{d}\boldsymbol{v}}{\mathrm{d}t} = \frac{1}{\rho}\nabla\cdot\boldsymbol{\sigma}\,, \tag{2}$$

$$\frac{\mathrm{d}U}{\mathrm{d}t} = -\frac{P}{\rho}\mathrm{Tr}\,\dot{\boldsymbol{\epsilon}} + \frac{1}{\rho}\boldsymbol{S}:\dot{\boldsymbol{\epsilon}}\,, \tag{3}$$

$$\frac{\mathrm{d}\boldsymbol{S}}{\mathrm{d}t} = 2\mu\left(\dot{\boldsymbol{\epsilon}} - \tfrac{1}{3}\mathbf{1}\,\mathrm{Tr}\,\dot{\boldsymbol{\epsilon}}\right), \tag{4}$$

supplemented by Tillotson equation of state (Tillotson, 1962). The notation is as follows: ρ is the density, $\boldsymbol{v}$ the velocity, $\boldsymbol{\sigma}$ the stress tensor (total), $\boldsymbol{\sigma} \equiv -P\mathbf{1} + \boldsymbol{S}$, P the pressure, $\mathbf{1}$ the unit tensor, $\boldsymbol{S}$ the deviatoric stress tensor, U the specific internal energy, $\dot{\boldsymbol{\epsilon}}$ the strain rate tensor, $\dot{\boldsymbol{\epsilon}} \equiv \frac{1}{2}\left[\nabla\boldsymbol{v} + (\nabla\boldsymbol{v})^{\mathrm{T}}\right]$, its trace being equal to $\mathrm{Tr}\,\dot{\boldsymbol{\epsilon}} = \nabla\cdot\boldsymbol{v}$, μ the shear modulus.

The model includes both elastic and plastic deformation, namely the yielding criterion of von Mises (1913) — given by the factor $f \equiv \min[Y_0^2/(\frac{3}{2}\boldsymbol{S}:\boldsymbol{S}), 1]$ — and also failure of the material. Initial distribution of cracks and their growth to fractures is described by models of Weibull (1939) and Grady and Kipp (1980), which use a scalar parameter $\mathcal{D} \in \langle 0, 1\rangle$ called damage, as explained in Benz and Asphaug (1994). The stress tensor of damaged material is then modified as $\boldsymbol{\sigma} = -(1-\mathcal{D}H(-P))P\mathbf{1} + (1-\mathcal{D})f\boldsymbol{S}$, where $H(x)$ denotes Heaviside step function. In this phase, we neglect the influence of gravity, which is a major simplification of the problem.

In a smoothed-particle hydrodynamic (SPH) formalism, Eqs. (1) to (4) are rewritten so as to describe an evolution of individual SPH particles (denoted by the index $i = 1..N$):

$$\frac{\mathrm{d}\rho_i}{\mathrm{d}t} = -\rho_i\sum_j \frac{m_j}{\rho_j}(\boldsymbol{v}_j - \boldsymbol{v}_i)\cdot\nabla W_{ij}\,, \tag{5}$$

$$\frac{\mathrm{d}\boldsymbol{v}_i}{\mathrm{d}t} = \sum_j m_j\left(\frac{\boldsymbol{\sigma}_i + \boldsymbol{\sigma}_j}{\rho_i\rho_j}\right)\cdot\nabla W_{ij}\,, \tag{6}$$

$$\frac{\mathrm{d}U_i}{\mathrm{d}t} = -\frac{P_i}{\rho_i}\sum_\gamma \dot{\epsilon}_i^{\gamma\gamma} + \frac{1}{\rho_i}\sum_\alpha\sum_\beta S_i^{\alpha\beta}\dot{\epsilon}_i^{\alpha\beta}\,, \tag{7}$$

$$\frac{\mathrm{d}\boldsymbol{S}_i}{\mathrm{d}t} = 2\mu\left(\dot{\boldsymbol{\epsilon}}_i - \tfrac{1}{3}\mathbf{1}\sum_\gamma \dot{\epsilon}_i^{\gamma\gamma}\right), \tag{8}$$

with:

$$\dot{\epsilon}_i^{\alpha\beta} = \frac{1}{2\rho_i}\sum_j m_j\left[(v_j^\alpha - v_i^\alpha)\frac{\partial W_{ij}}{\partial x^\beta} + (v_j^\beta - v_i^\beta)\frac{\partial W_{ij}}{\partial x^\alpha}\right], \tag{9}$$

where m_j denote the masses of the individual SPH particles, $W_{ij} \equiv W(|\boldsymbol{r}_i - \boldsymbol{r}_j|, h)$ the kernel function, a B-spline M_4 in our case, h the symmetrized smoothing length, $h = \frac{1}{2}(h_i + h_j)$. Both the equation of motion and the energy equation were also supplied with the standard artificial viscosity term Π_{ij} (Monaghan and Gingold, 1983) with coefficients $\alpha_{\rm AV} = 1.5$,

$\beta_{\mathrm{AV}} = 3$. We sum over all particles, but since the kernel has a compact support, the algorithm has an asymptotic complexity $O(NN_{\mathrm{neighbours}})$. The actual number of SPH particles we used is $N \doteq 1.4 \times 10^5$, the number of neighbours is usually $N_{\mathrm{neighbours}} \simeq 50$. There is also a evolution equation for the smoothing length h_i in order to adapt to varying distances between SPH particles.

2.2. Hand-off procedure

Although the SPH is a versatile method suitable for simulating both the fragmentation and the gravitational reaccumulation, the time step of the method is bounded by Courant criterion and the required number of time steps for complete reaccumulation is prohibitive. In order to proceed with inevitably simplified but efficient computations, we have to convert SPH particles to solid spheres, a procedure called hand-off. In this paper, we compute the corresponding radius R_i as:

$$R_i = \left(\frac{3m_i}{4\pi\rho_i} \right)^{\frac{1}{3}} . \tag{10}$$

The time t_{handoff} at which the hand-off takes place is determined by three conditions:

1. It has to be at least $2D_{\mathrm{PB}}/c_{\mathrm{s}} \simeq 1\,\mathrm{s}$, until the shock wave and rarefaction wave propagate across the target;
2. Fractures (damage) in the target should not propagate anymore, even though in catastrophic disruptions the shock wave usually damages the whole target and material is then practically strength-less;
3. The pressure in the fragmented parent body should be zero so that the corresponding acceleration $-\frac{1}{\rho}\nabla P$ is zero, or at least negligible. According to our tests for $D_{\mathrm{PB}} = 10\,\mathrm{km}$ targets, such relaxation takes up to 10 s.

On the other hand, there is an upper limit for t_{handoff} given by the gravitational acceleration of the target, $g = GM_{\mathrm{PB}}/R_{\mathrm{PB}}^2$, which has to be small compared to the escape velocity $v_{\mathrm{esc}} = \sqrt{2GM_{\mathrm{PB}}/R_{\mathrm{PB}}}$, i.e. a typical ejection velocity v_{ej} of fragments. The corresponding time span should thus be definitely shorter than $v_{\mathrm{esc}}/g \simeq 10^3$ s.

2.3. Reaccumulation phase

Finally, gravitational reaccumulation of now spherical fragments is computed with an N-body approach. We use `pkdgrav` code by Richardson et al. (2000) for this purpose. It accounts for mutual gravitational interactions between fragments:

$$\ddot{\boldsymbol{r}}_i = -\sum_{j \neq i} \frac{Gm_j}{r_{ij}^3} \boldsymbol{r}_{ij} , \tag{11}$$

An $O(N^2)$ problem is simplified significantly using the Barnes–Hut algorithm, i.e. by clustering fragments to cells and evaluating gravitational moments up to hexadecapole order, provided they fit within the opening angle $\mathrm{d}\theta = 0.5\,\mathrm{rad}$. The time step was $\Delta t = 10^{-6}$ (in $G = 1$ units, or about 5 s in SI), and the time span $50,000\,\Delta t$, long enough that the reaccumulation is over, or negligible.

Regarding mutual collisions, we assumed a perfect sticking only, it means no restitution coefficients, bouncing or friction. Consequently, we have no information about resulting shapes of fragments, we rather focus on their sizes, velocities and corresponding statistics.

3. A grid of simulations for $D_{\mathrm{PB}} = 10\,\mathrm{km}$ targets

We performed a number of simulations with $D_{\mathrm{pb}} = 10\,\mathrm{km}$ parent bodies, impact velocity v_{imp} varying from 3 to 7 km/s, diameter d_{project} of the impactor from 0.293 km to 1.848 km (with a logarithmic stepping) and the impact angle ϕ_{imp} from 15° to 75°. The kinetic energy of the impact:

$$Q = \frac{\frac{1}{2} m_{\mathrm{project}} v_{\mathrm{imp}}^2}{M_{\mathrm{pb}}} \tag{12}$$

therefore varies from $\sim 10^{-2} Q_{\mathrm{D}}^{\star}$ to $\sim 20 Q_{\mathrm{D}}^{\star}$, where $Q_{\mathrm{D}}^{\star}$ is the critical energy for shattering and dispersing 50% of the parent body. We adopted $Q_{\mathrm{D}}^{\star}(D)$ values for comparisons from the scaling law of Benz and Asphaug (1999). The total number of performed runs is 125. We assume a monolithic structure of both the target and the impactor, and the material properties were selected those of basalt (summarized in Table **??**).

3.1. Size-frequency distributions

For each run we constructed a cumulative size-frequency distributions $N(>D)$ of fragments and we plotted them in Figure B.6.

At first sight, the SFDs are well-behaved. Both cratering and catastrophic events produce mostly power-law-like distributions. Some distributions, mainly those around $Q/Q_{\mathrm{D}}^{\star} \sim 1$, have an increasing slope at small sizes (at around $D \sim 0.3\,\mathrm{km}$), but since this is close to the resolution limit, it is possibly a numerical artifact.

For supercatastrophic impacts with $d_{\mathrm{project}} = 1.848\,\mathrm{km}$, the distributions differ from power laws substantially; the slope becomes much steeper at large sizes of fragments. These are the cases where the gap between the largest remnant and the largest fragment disappears (we therefore say the largest remnant does not exist).

The situation is quite different for impacts with an oblique impact angle, mainly for $\phi_{\mathrm{imp}} = 75°$. We notice that these impacts appear much less energetic compared to other impact angles, even though the ratio $Q/Q_{\mathrm{D}}^{\star}$ is the same. The cause of this apparent discrepancy is simply the geometry of the impact. At high impact angles, the impactor does not hit the target with all its cross-section and a part of it misses the target entirely. Therefore, a part of the kinetic energy is not deposited into the target and the impact appears less energetic, compared to head-on impacts.

3.2. Velocity histograms

Similarly to the size-frequency distributions, we computed velocity distributions of fragments. The results are shown in Figure 2. As we are computing an absolute value of the velocity,

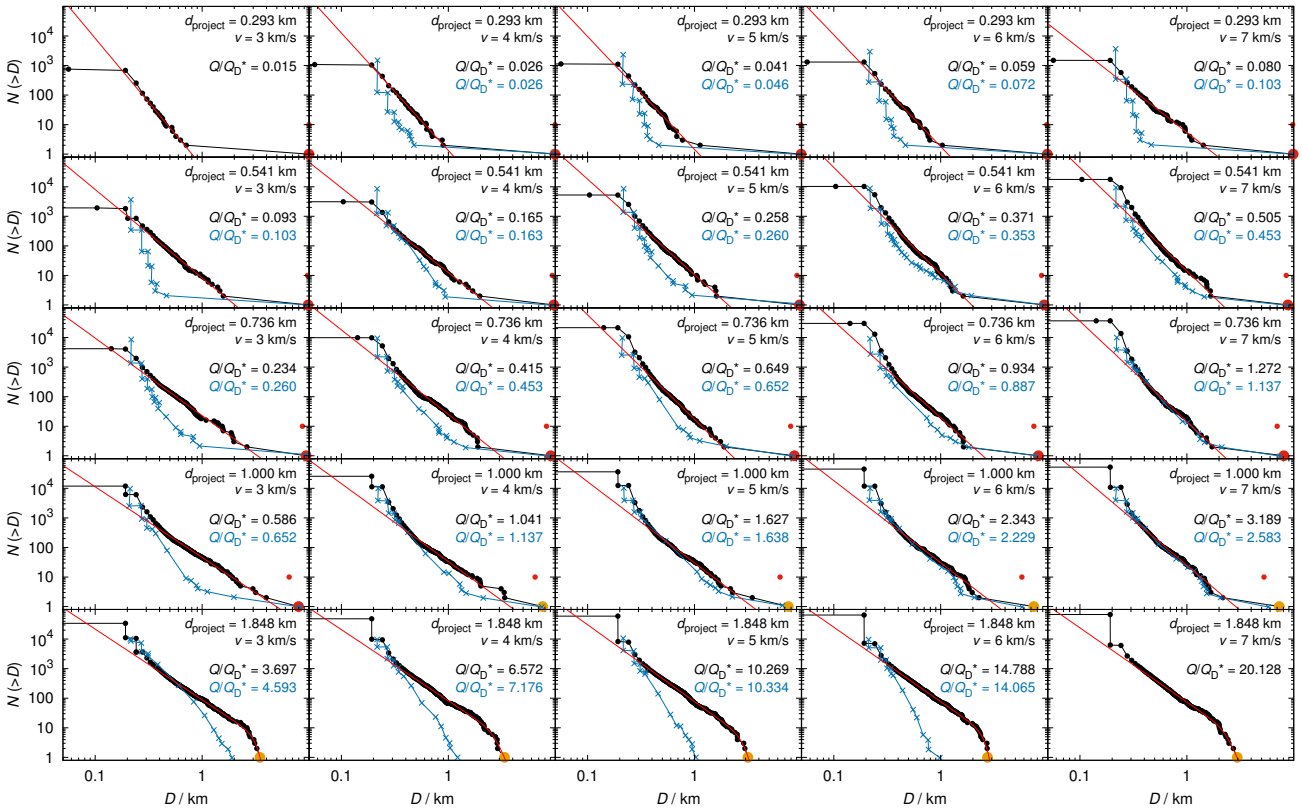

Figure 1: Cumulative size-frequency distributions $N(>D)$ of fragments ejected during disruptions of parent bodies with sizes $D_{\rm PB} = 10\,$km. The impact angle was $\phi_{\rm imp} = 45°$; results for different impact angles are shown on following pages. The projectile size is increasing downwards, from $d_{\rm project} = 0.293\,$km to $1.848\,$km, so that the logarithm of the mass ratio $\log_{10}(m_{\rm project}/M_{\rm PB}) = 3.0, 2.6, 2.2, 1.8$ and 1.0. The impact velocity is increasing to the right, from $v_{\rm imp} = 3$ to $7\,{\rm km\,s^{-1}}$. Both of the quantities are also indicated in individual panels, together with the ratio $Q/Q^\star_{\rm D}$ of the specific energy Q and strength $Q^\star_{\rm D}$ inferred from the scaling law of Benz and Asphaug (1999). Largest remnant size $D_{\rm LR}$ is coloured red or orange for cratering or catastrophic events, respectively. For a discussion of scaling we overplot simulated SFD's from Durda et al. (2007) computed for disruptions of $D_{\rm PB} = 100\,$km targets and scaled down by dividing sizes by a factor 10 (blue lines and labels). To compare 'apples with apples', we compare runs with (approximately) the same $Q/Q^\star_{\rm D}$ ratios and the same impact angle. For some impact parameters, the scaled SFD is missing as there is no run in the dataset of Durda et al. with comparable $Q/Q^\star_{\rm D}$. Finally, the red curve is the fit of a suitable function, used to derive parametric relations (see Section 4).

the resulting histogram depends on a selected reference frame. We chose a barycentric system for all simulations; however, we excluded high-velocity remainders of the projectile with velocities $v_{\rm ej} > v_{\rm cut} \equiv 1\,{\rm km/s}$. These outliers naturally appear mainly for oblique impact angles. Because of very large ejection velocities, such fragments cannot belong to observed families and if we had included them in the constructed velocity field of the synthetic family, it would artificially shift velocities of fragments to higher values.

The main feature of cratering events is the peak around the escape velocity $v_{\rm esc}$. This peak is created by fragments ejected at the point of impact. With an increasing impact energy, the tail of the histogram extends as the fragments are ejected at higher velocities.

Interestingly, there appears a second peak at around $Q/Q^\star_{\rm D} \sim 0.3$. This is because of ejection of fragments from the antipode of the target. If the shockwave is energetic enough, it causes an ejection of many fragments. The second peak is barely visible at oblique impact angles.

3.3. Isotropy vs anisotropy of the velocity field

Figure 3 shows angular distributions of the velocity fields in the plane of the impact. The histograms are drawn as polar plots with a 5° binning. The labels of angles correspond to the impact angles $\phi_{\rm imp}$, as we can see on cratering events, where the distribution is nicely clustered around $\phi_{\rm imp}$.

Cratering impacts tend to produce velocity fields mainly in the direction of the impact angle. Catastrophic impacts, on the other hand, generally produce much more isotropic velocity fields. However, the isotropy is not perfect, even though we removed outliers as above. Even for the supercatastrophic impacts, the number of fragments in different directions can vary by a factor of 5. Further changes of the reference frame may improve the isotropy; not that for observed families, it is also not clear where is the reference points, because the identification of all family members (and interlopers) is not unambiguous.

...

3.4. A comparison with scaled-down $D_{\rm PB} = 100\,$km simulations

The mid-energy events with $Q/Q^\star_{\rm D} \sim 1$ have SFDs comparable to scaled 100km ones. In this regime, down-scaling of distribution for $D_{\rm pb} = 100\,$km targets seems to be a justifiable way to approximate SFDs for targets of smaller size.

In case of cratering events, however, our simulations differ significantly from scaled ones. Impacts into 10km targets produce a much shallower fragment distribution compared to 100km impacts; see impacts with $d_{\rm project} = 0.293\,$km. We also note that supercatastrophic runs have different outcomes than the 100km ones as well; our distributions are much shallower and have a much larger largest fragment. They also have a steeper part of SFD at larger diameters, which is *not* visible for 100km simulations, at least not to the same extent.

4. Parametric relations for Monte-Carlo collisional models

Size-frequency distributions constructed from our simulations mostly have a shape of the power law with a separated largest remnant. The slope of the distribution in a log-log plot can be therefore fitted with a linear function:

$$\log N(>D) = q \log[D]_{\rm km} + c\,. \tag{13}$$

Supercatastrophic events behave differently though, and their SFDs can be well fitted with a two-slope function:

$$\log N(>D) = K\left(\log[D]_{\rm km} - \log[D_0]_{\rm km}\right) + c\,, \tag{14}$$

where:

$$K(x) = \frac{1}{2}(q_1+q_2)x + \frac{1}{2}\frac{q_1-q_2}{k}\log\left(2\cosh kx\right)\,. \tag{15}$$

In this approximation of SFD, the q_1 and q_2 are the limit slopes for $D \to \infty$ and $D \to 0$, respectively, and k characterizes the "bend-off" of the function. Because of the problems with a convergence of the fit, we fix $k = 10$ and perform the fit using only four parameters: s_1, s_2, D_0 and c.

Because impacts at high angles appear weaker due to the geometry (see Section 3.1), we have to account for the actual kinetic energy delivered into the target. We modify the specific impact energy Q by a ratio of the cross-sectional area of the impact and the total area of the impactor. This can be easily computed from the geometry of the impact, using a formula for circle-circle intersection: let R be the radius of the target, r the radius of the projectile and d a projected distance between their centers. The area of impact is then given by:

$$A = r^2\cos^{-1}\left(\frac{d^2+r^2-R^2}{2dr}\right) + R^2\cos^{-1}\left(\frac{d^2+R^2-r^2}{2dR}\right) - \\ - \frac{1}{2}\sqrt{(R+r-d)(d+r-R)(d-r+R)(d+r+R)}\,. \tag{16}$$

As both spheres touch at the point of the impact, we have:

$$d = (r+R)\sin\phi_{\rm imp}\,. \tag{17}$$

Using these auxiliary quantities, we define *effective* specific impact energy:

$$Q_{\rm eff} = Q\frac{A}{\pi r^2}\,. \tag{18}$$

In Figure 4, we separately plot slopes q, constants c of the linear fitis of SFDs, and the masses of largest remnants $M_{\rm lr}$ and largest fragment $M_{\rm lf}$. Each of these quantities shows a distinct dependence on the impact velocity $v_{\rm imp}$, suggesting parametric relations cannot be well described by a single parameter $Q_{\rm eff}/Q_{\rm D}$. We therefore plot each dependence separately for different $v_{\rm imp}$ and we explicitly express the dependence on $v_{\rm imp}$ in parametric relations.

For low velocities, slopes q can be reasonably fitted with a function:

$$q = -12.3 + 0.75 v_{\rm imp} + \frac{(11.5 - 1^{+0.2}_{-0.1} v_{\rm imp})\exp\left(-5\cdot 10^{-3}\dfrac{Q_{\rm eff}}{Q^\star_{\rm D}}\right)}{1 + 0.1^{+0.01}_{-0.02}\left(\dfrac{Q_{\rm eff}}{Q^\star_{\rm D}}\right)^{-0.4}}, \tag{19}$$

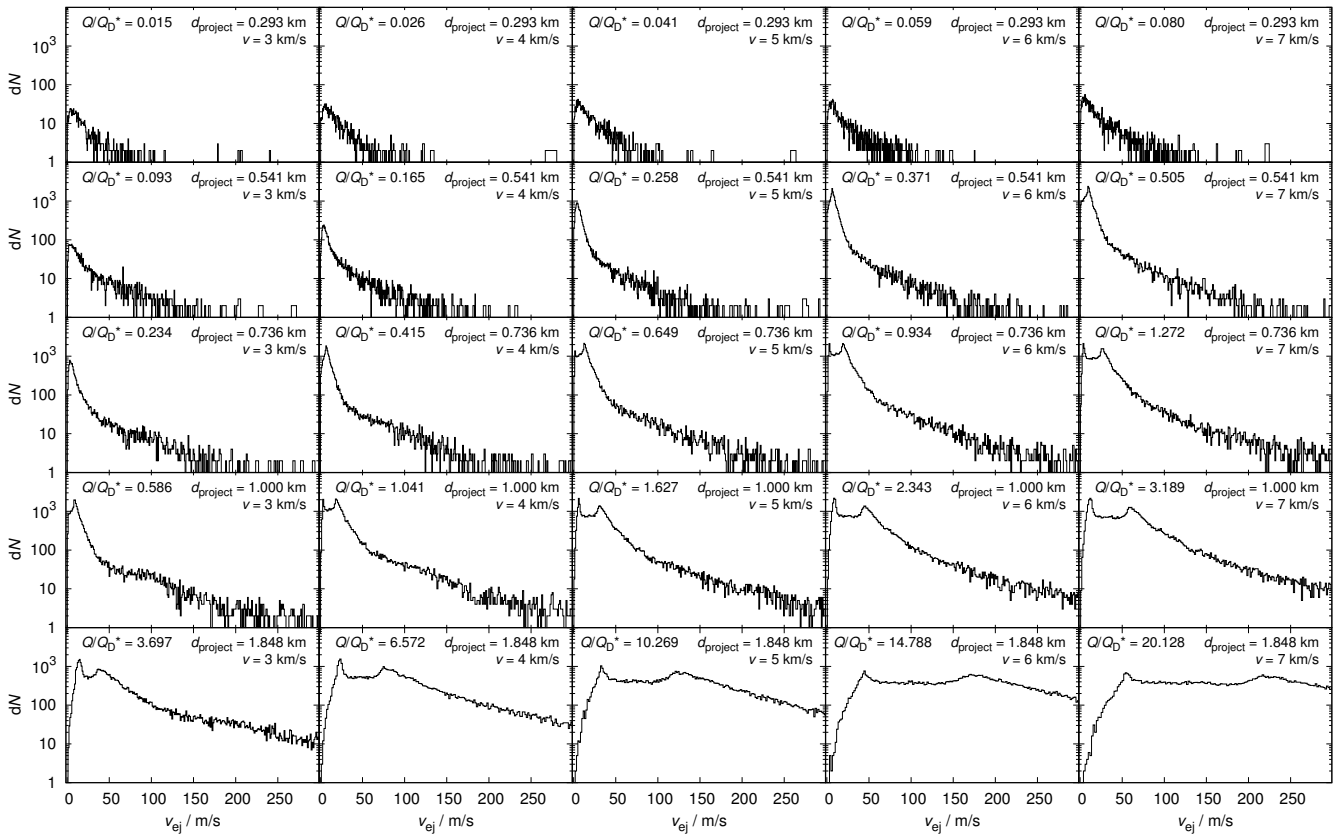

Figure 2: Differential histograms dN of ejection velocities $v_{\rm ej}$ of fragments for the same set of simulations as in Figure B.6. The velocity is computed in a barycentric reference frame with outliers ($v_{\rm imp} > 1$ km/s) are removed as they are mostly remnants of the projectile. The escape velocity from the target $D_{\rm PB} = 10$ km in size is $v_{\rm esc} = 6.1\,{\rm m\,s^{-1}}$ and so are the histograms peaks of the order of several $v_{\rm esc}$, at least for the majority of simulations. However, there is also a significant second peak visible. It is close to the first peak for cratering to mid-energy impacts and extends to velocities $v_{\rm ej} > 100$ m/s for supercatastrophic breakups with $Q/Q^{\star}_{\rm D} \gtrsim 10$. The impact angle $\phi_{\rm imp} = 45^{\circ}$ in this case.

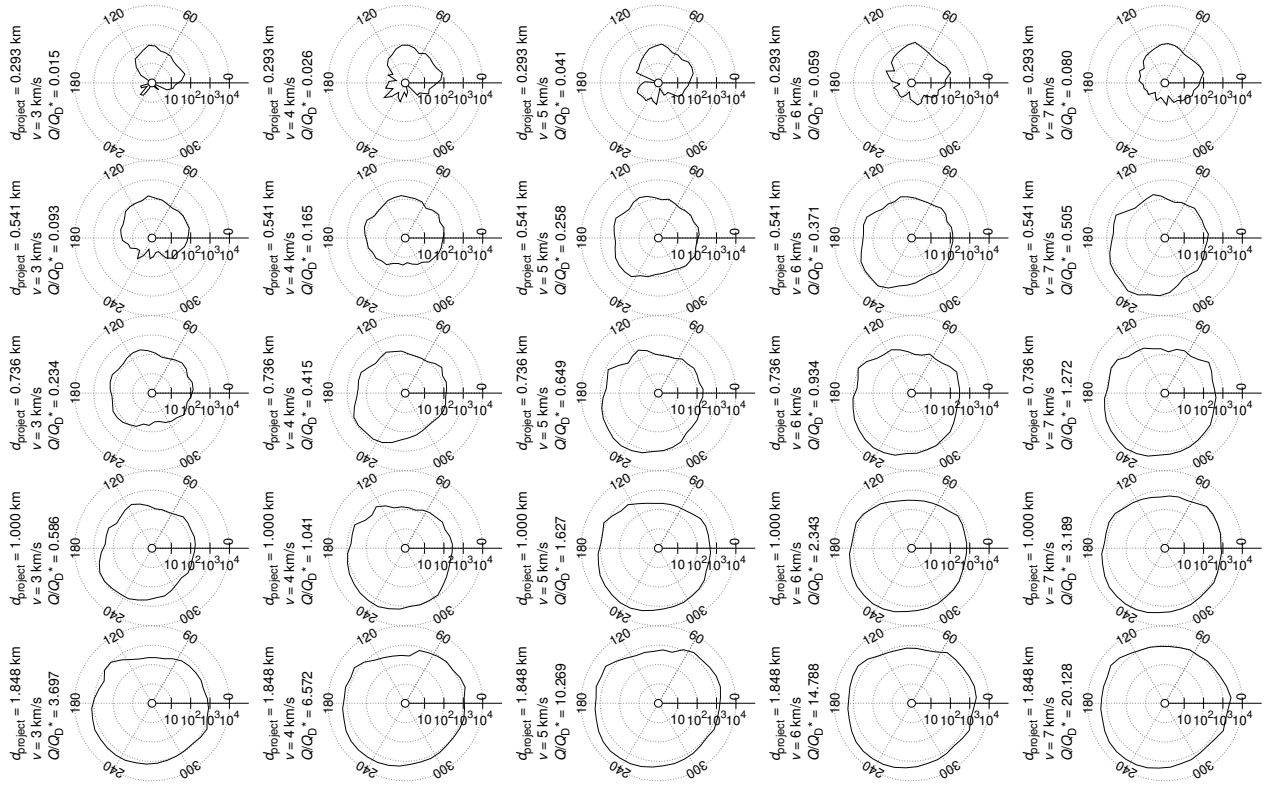

Figure 3: Histograms of velocity angular distribution (in the plane of the collision) of fragments. The velocities are evaluated in the barycentric coordinate system with outliers removed. The angle 180° corresponds to the velocity direction of the projectile. The impact angle $\phi_{\rm imp} = 45°$.

where $v_{\rm imp}$ is expressed in km/s. However, for high velocities (especially for $v = 7$ km/s), the individual values of q for different impact angles differ significantly and thus the fit has a very high uncertainty. We account for this behaviour in Eq. (19), where the uncertainty increases with an increasing velocity.

The constant c can be well fitted with line in this plot:

$$c = 0.9 + 2.3\exp(-0.35 v_{\rm imp}) + \left(1.3 - 0.1 v_{\rm imp}\right)\left(\frac{Q_{\rm eff}}{Q_{\rm D}^{\star}}\right). \quad (20)$$

The high scatter noted in the parametric relation for the slope q is not present here. This parameter is of lesser importance for Monte-Carlo models though, as the distribution must be normalized anyway to conserve the total mass.

Largest remnants are also plotted in Figure 4. Notice that some points are missing here as the largest remnant does not exist for supercatastrophic impacts. As we are using the effective impact energy $Q_{\rm eff}$ as an independent variable, the runs with impact angle $\phi = 75°$ produce largest remnants of sizes comparable to other impact angles. This helps to decrease the scatter of points and make the derived parametric relation more accurate. We selected a fitting function:

$$M_{\rm lr} = \frac{M_{\rm tot}}{1 + \left[0.6^{+0.5}_{-0.2} + 56\exp(-1.0^{+0.6}_{-0.2} v_{\rm imp})\right]\left(\frac{Q_{\rm eff}}{Q_{\rm D}^{\star}}\right)^{0.8+8\exp(-0.7 v_{\rm imp})}}. \quad (21)$$

Largest fragments (fourth row) exhibit a larger scatter, similarly as the slopes q. The masses of the largest fragment can differ by an order of magnitude for different impact angles (notice the logarithmic scale on y-axis). Nevertheless, the values averaged over impact angles (red circles) lie close the fit in most cases. The fitting function in this case is:

$$M_{\rm lf} = \frac{M_{\rm tot}}{0.24^{+0.60}_{-0.15} v_{\rm imp}^3 \left(\frac{Q_{\rm eff}}{Q_{\rm D}^{\star}}\right)^{-0.6-2\exp(-0.3 v_{\rm imp})} + \exp\left(-0.3^{+0.2}_{-0.2} v_{\rm imp}\right)\frac{Q_{\rm eff}}{Q_{\rm D}^{\star}} + 11^{+15}_{-8} + 2 v_{\rm imp}}. \quad (22)$$

This function bends and starts to decrease for $Q/Q_{\rm D}^{\star} \gg 1$. Even though this behaviour is not immediately evident from the plotted points, the largest fragment *must* become a decreasing function of impact energy in the supercatastrophic regime.

5. Conclusions and future work

Acknowledgements

The work of MB has been supported by the Grant Agency of the Czech Republic (grant no. 13-01308S)

Appendix A. Uncertainties related to SPH simulations

effects on resulting size-frequency distributions and ejection velocity histograms

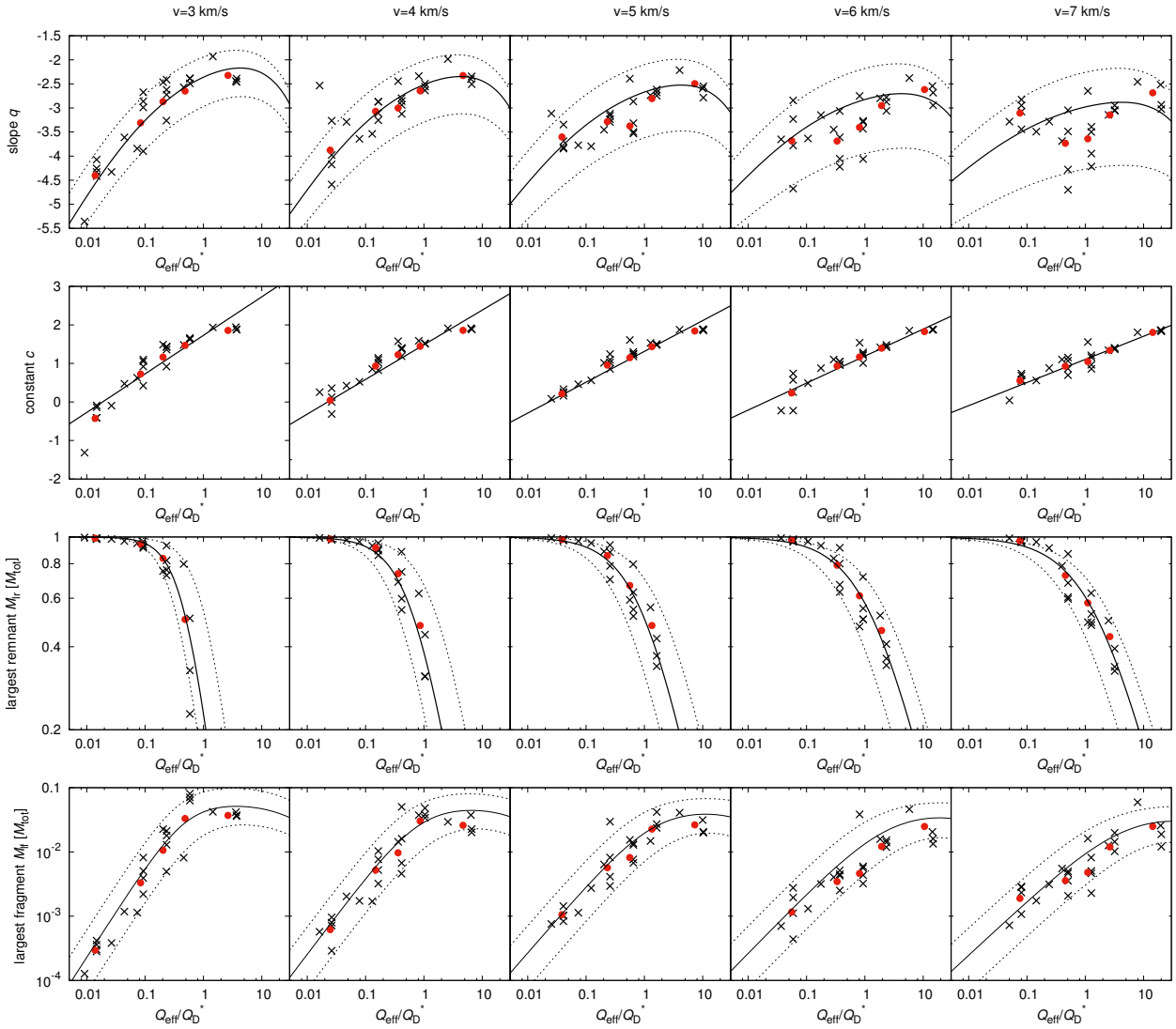

Figure 4: Parameters of the power-law fits of size-frequency distributions (first and second row) and masses of the largest remnant $M_{\rm lr}$ and the largest fragment $M_{\rm lf}$ (third and fourth row) as functions of the effective impact energy $Q_{\rm eff}/Q_{\rm D}^{\star}$, defined by Eq. (18). We plotted these quantities for each value of impact velocity separately as considering $Q_{\rm eff}/Q_{\rm D}^{\star}$ as a single parameter would imply a large variance of data and therefore a large uncertainty of parametric relations. Each black cross represents one SPH/N-body simulation, the red circles are given by averaging over impact angles $\phi_{\rm imp}$. The data are fitted with suitable functions and the scatter of values propagates to the parametric relations as uncertainties, see Section 4.

in order to understand uncertainties in applications related to asteroid families and determination of parent body sizes

Appendix A.1. Time step or Courant criterion

Appendix A.2. Initial distribution of SPH particles

For a unique solution of evolutionary differential equations, initial conditions have to be specified. In our case, this means setting the initial positions and velocities of SPH particles. Velocities are easily determined, all particles of the target are at rest, all particles of the impactor move with the velocity of the impactor.

Optimal initial positions of SPH particles have to meet several criteria. First of all, the distribution needs to have low discrepancy. This requirement eliminates a random distribution as a suitable method, for using such distribution would necessarily lead to clustering particles in some parts of space and a lack of particles in other parts. Interpolation properties of random distribution are very poor and result in high numerical uncertainties of the method.

We therefore use a hexagonally close lattice packing in the simulations. They are easily set up and have an optimal interpolation accuracy. However, no lattice is *isotropic*, there are always preferred directions in the distribution of SPH particles. This could potentially lead to numerical artifacts, such as pairing instability (Herant, 1994). Also, the resolution of the lattice distribution is uniform, the impact is therefore resolved by only few SPH particles for small impactors. We can increase accuracy of cratering impacts by distribution SPH particles nonuniformly, putting more particles to the point of impact and less to more distant places.

Here we assess an uncertainty introduced by using different initial conditions of SPH particles. A suitable method for generating a nonuniform isotropic distribution with low discrepancy has been described by Diehl et al. (2012) and Rosswog (2015). Using initial conditions generated by this method, we run several SPH/N-body simulations, and we compare the results to the simulations with lattice initial conditions.

The comparison is in Figure A.5. Generally, the target shatters more for the nonuniform distribution. The largest remnant is smaller, the difference is up to 10% for performed simulations. There are also more fragments at larger diameters, compared to lattice distribution. This is probably due to slightly worse interpolation properties of the nonuniform distribution. A test run for a *random* distribution of particles led to a complete disintegration of the target and a largest remnant smaller by an order of magnitude, suggesting the smaller largest remnant is a numerical artifact of the method. On the other hand, the SFD is comparable at smaller diameters. This leads to more bent, less power-law-like SFDs for nonuniform runs.

Appendix A.3. The number of SPH particles for target and projectile

Appendix A.4. Computation of radii corresponding to SPH particles (hand-off)

Appendix A.5. Total damage and putative formation of dust clouds

Appendix B. Figure

References

Benavidez, P. G., Durda, D. D., Enke, B. L., Bottke, W. F., Nesvorný, D., Richardson, D. C., Asphaug, E., Merline, W. J., May 2012. A comparison between rubble-pile and monolithic targets in impact simulations: Application to asteroid satellites and family size distributions. Icarus 219, 57–76.

Benz, W., Asphaug, E., Jan. 1994. Impact simulations with fracture. I - Method and tests. Icarus 107, 98.

Benz, W., Asphaug, E., Nov. 1999. Catastrophic Disruptions Revisited. Icarus 142, 5–20.

Cibulková, H., Brož, M., Benavidez, P. G., Oct. 2014. A six-part collisional model of the main asteroid belt. Icarus 241, 358–372.

Cossins, P. J., 2010. The Gravitational Instability and its Role in the Evolution of Protostellar and Protoplanetary Discs. Ph.D. thesis, University of Leicester.

Davis, D. R., Ryan, E. V., 1990. On collisional disruption: Experimental results and scaling laws. Icarus 83 (1), 156 – 182.

Diehl, S., Rockefeller, G., Fryer, C. L., Riethmiller, D., Statler, T. S., Nov. 2012. Generating Optimal Initial Conditions for Smooth Particle Hydrodynamics Simulations. ArXiv e-prints.

Durda, D. D., Bottke, W. F., Nesvorný, D., Enke, B. L., Merline, W. J., Asphaug, E., Richardson, D. C., Feb. 2007. Size-frequency distributions of fragments from SPH/N-body simulations of asteroid impacts: Comparison with observed asteroid families. Icarus 186, 498–516.

Grady, D., Kipp, M., 1980. Continuum modelling of explosive fracture in oil shale. International Journal of Rock Mechanics and Mining Sciences & Geomechanics Abstracts 17 (3), 147 – 157.

Herant, M., 1994. Dirty Tricks for SPH (Invited paper) 65, 1013.

Herrmann, W., 1969. Constitutive equation for the dynamic compaction of ductile porous materials. Journal of Applied Physics 40 (6).

Hirayama, K., Oct. 1918. Groups of asteroids probably of common origin. AJ31, 185–188.

Jutzi, M., Holsapple, K., Wünneman, K., Michel, P., Feb. 2015. Modeling asteroid collisions and impact processes. Asteroids IV.

Michel, P., Benz, W., Paolo, T., Richardson, D. C., 2001. Collisions and gravitational reaccumulation: Forming asteroid families and satellites. Science 294 (5547), 1696–1700.

Michel, P., Benz, W., Richardson, D. C., Feb. 2003. Disruption of fragmented parent bodies as the origin of asteroid families. Nature 421, 608–611.

Michel, P., Benz, W., Richardson, D. C., Apr. 2004. Catastrophic disruption of pre-shattered parent bodies. Icarus 168, 420–432.

Michel, P., Jutzi, M., Richardson, D. C., Benz, W., Jan. 2011. The Asteroid Veritas: An intruder in a family named after it? Icarus 211, 535–545.

Michel, P., Tanga, P., Benz, W., Richardson, D. C., 2002. Formation of asteroid families by catastrophic disruption: Simulations with fragmentation and gravitational reaccumulation. Icarus 160 (1), 10 – 23.

Monaghan, J., Gingold, R., 1983. Shock simulation by the particle method sph. Journal of Computational Physics 52 (2), 374 – 389.

Morbidelli, A., Bottke, W. F., Nesvorný, D., Levison, H. F., Dec. 2009. Asteroids were born big. Icarus 204, 558–573.

Nakamura, A., Fujiwara, A., Jul. 1991. Velocity distribution of fragments formed in a simulated collisional disruption. Icarus 92, 132–146.

Nesvorný, D., Brož, M., Carruba, V., Feb. 2015. Identification and Dynamical Properties of Asteroid Families. Asteroids IV.

Nesvorný, D., Enke, B. L., Bottke, W. F., Durda, D. D., Asphaug, E., Richardson, D. C., Aug. 2006. Karin cluster formation by asteroid impact. Icarus 183, 296–311.

Price, D. J., Dec. 2008. Modelling discontinuities and Kelvin Helmholtz instabilities in SPH. Journal of Computational Physics 227, 10040–10057.

Price, D. J., Feb. 2012. Smoothed particle hydrodynamics and magnetohydrodynamics. Journal of Computational Physics 231, 759–794.

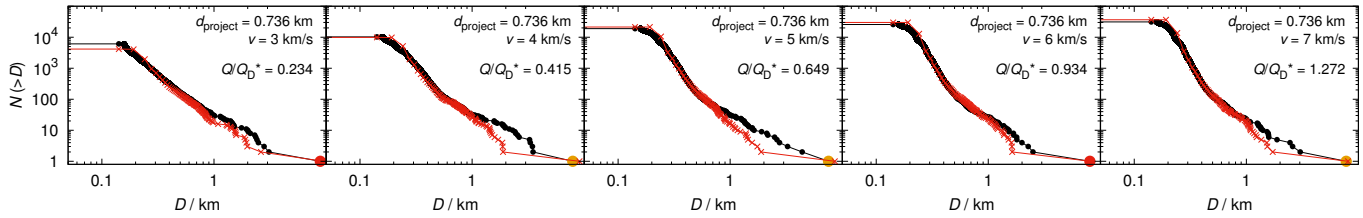

Figure A.5: Black histogram shows the runs with the nonuniform distribution generated by the method of Diehl et al. (2012), red are the previous (lattice) results shown in Figure B.6.

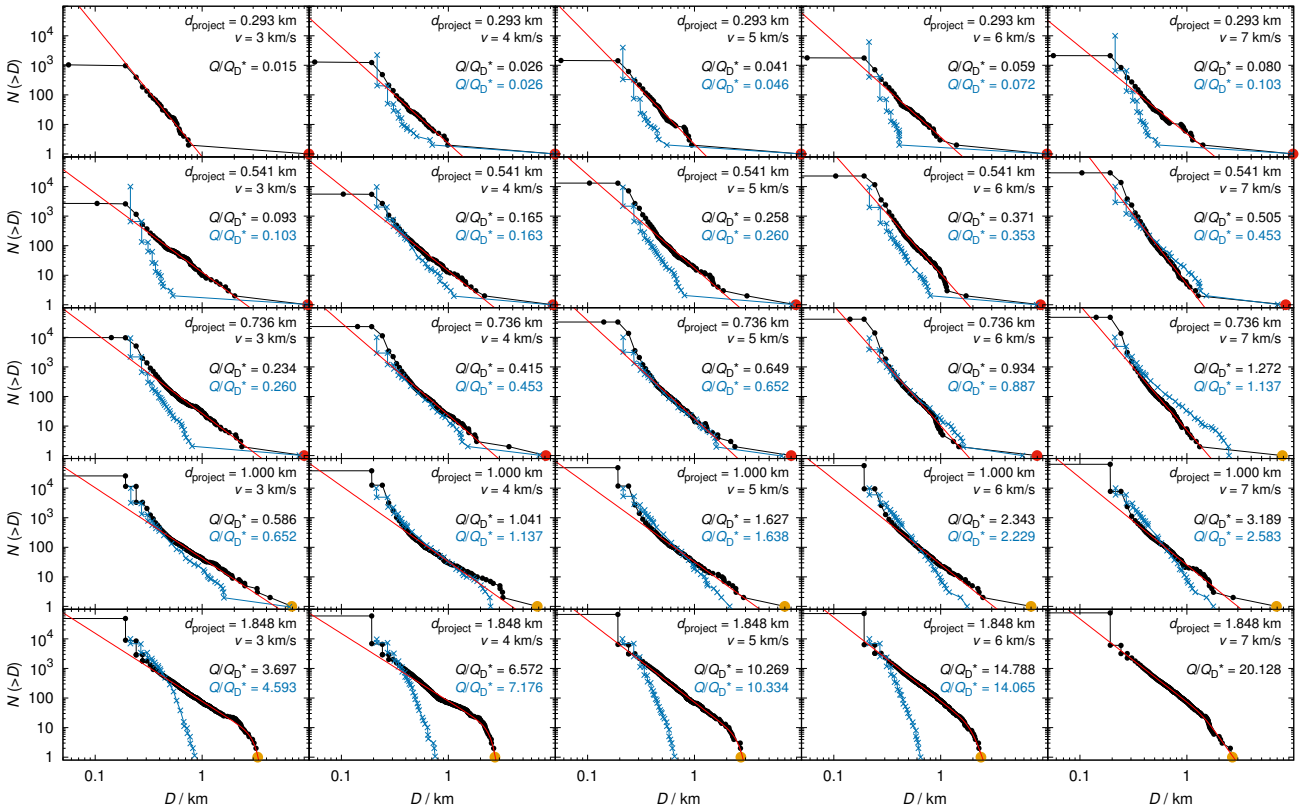

Figure B.6: Impact angle 15°.

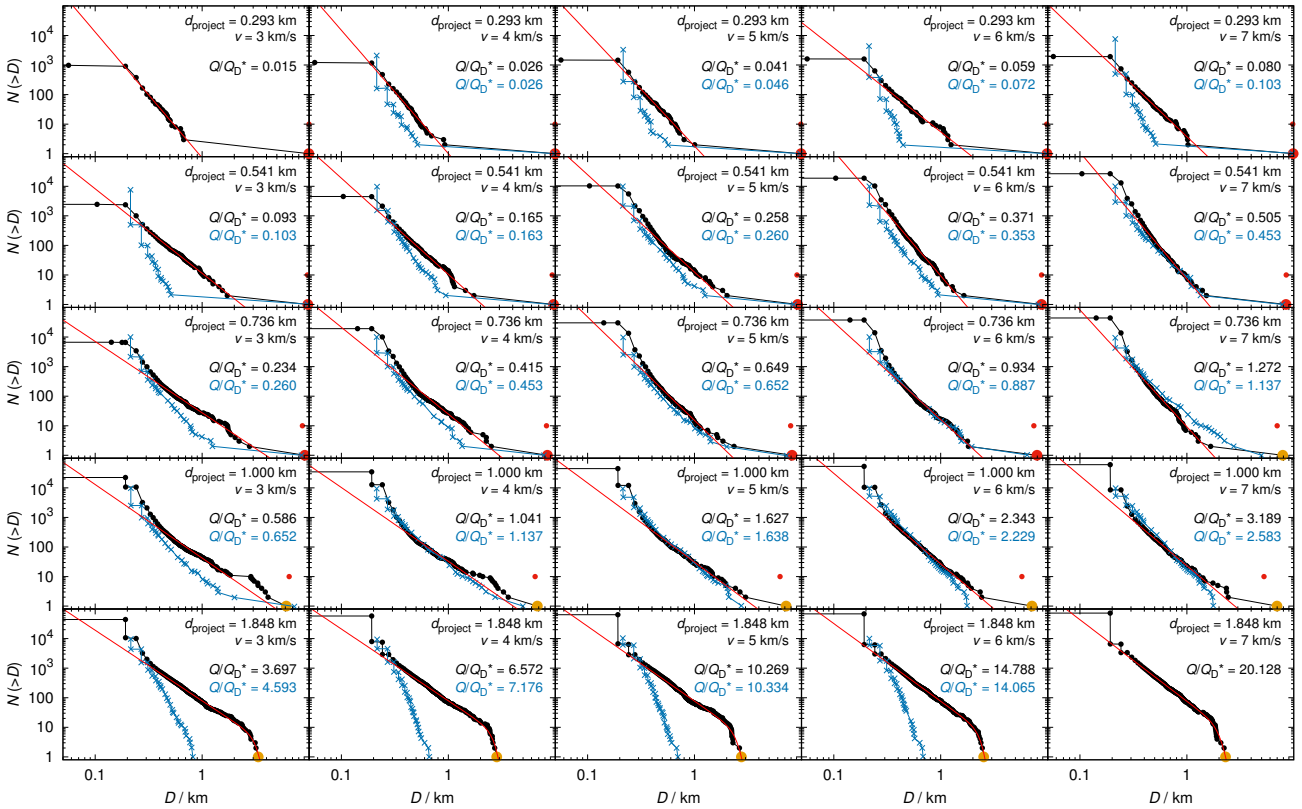

Figure B.7: Impact angle 30°

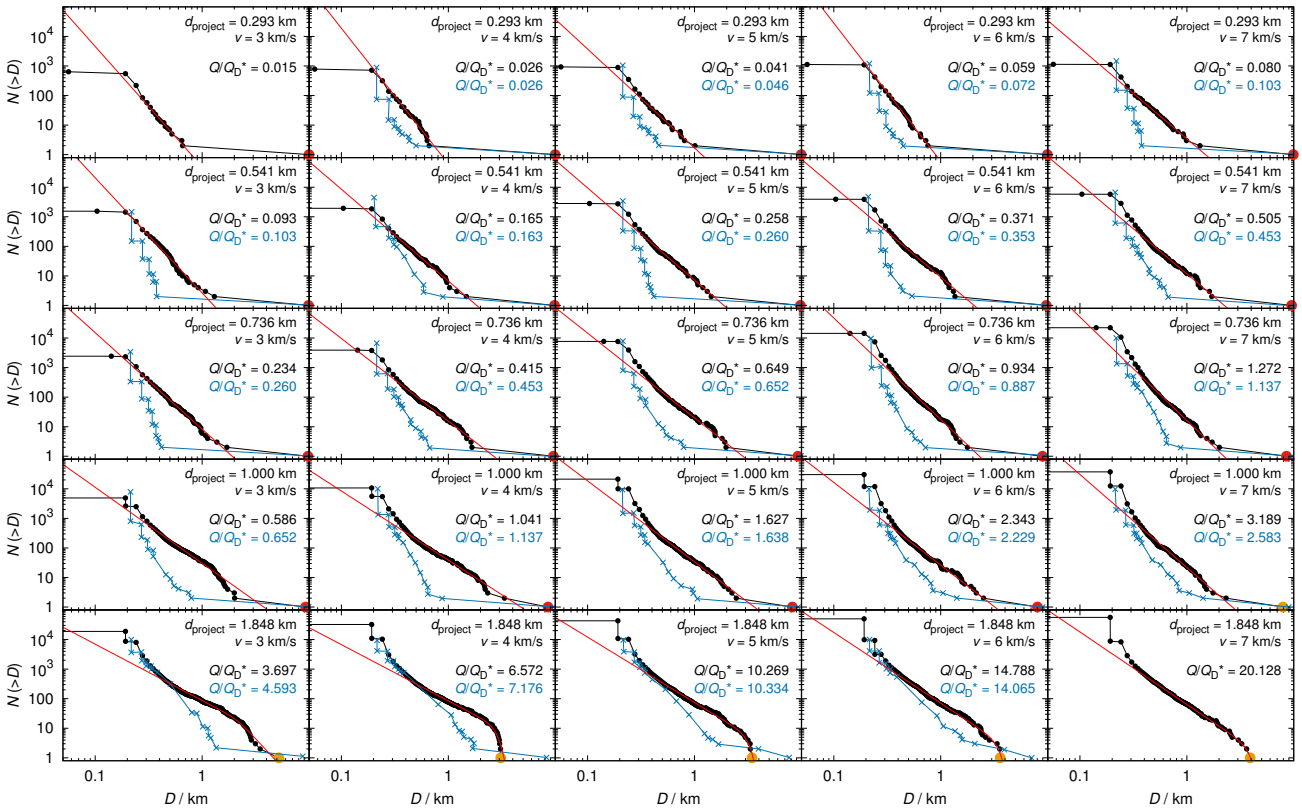

Figure B.8: Impact angle 60°.

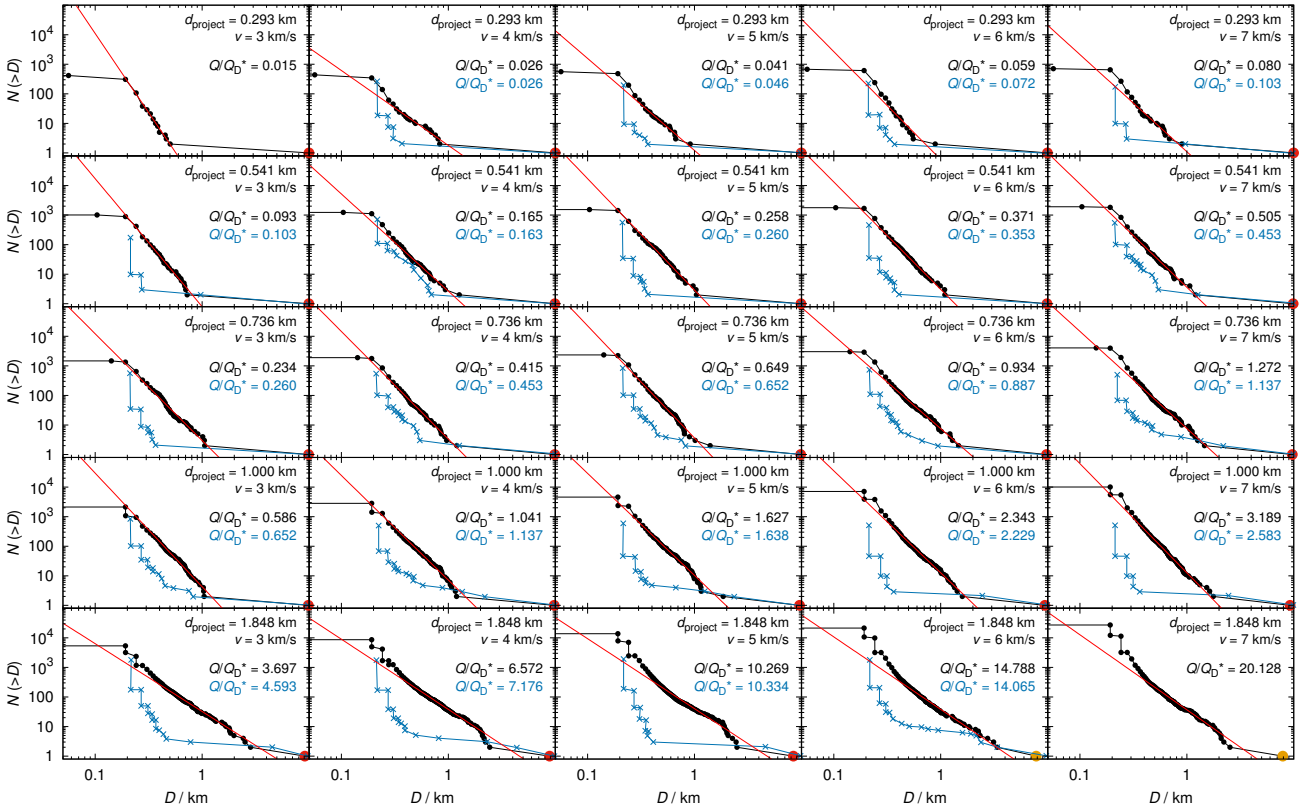

Figure B.9: Impact angle 75°.

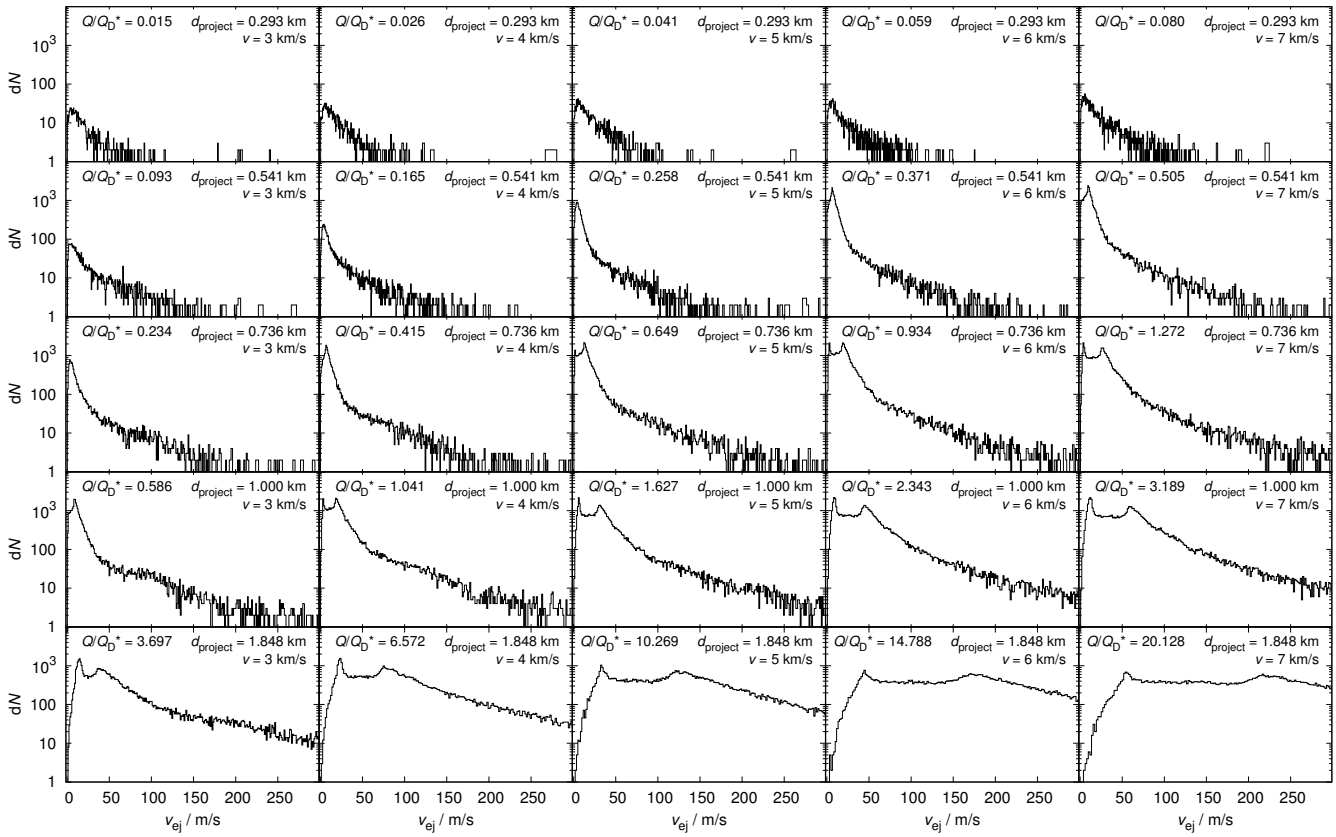

Figure B.10: Impact angle 15°

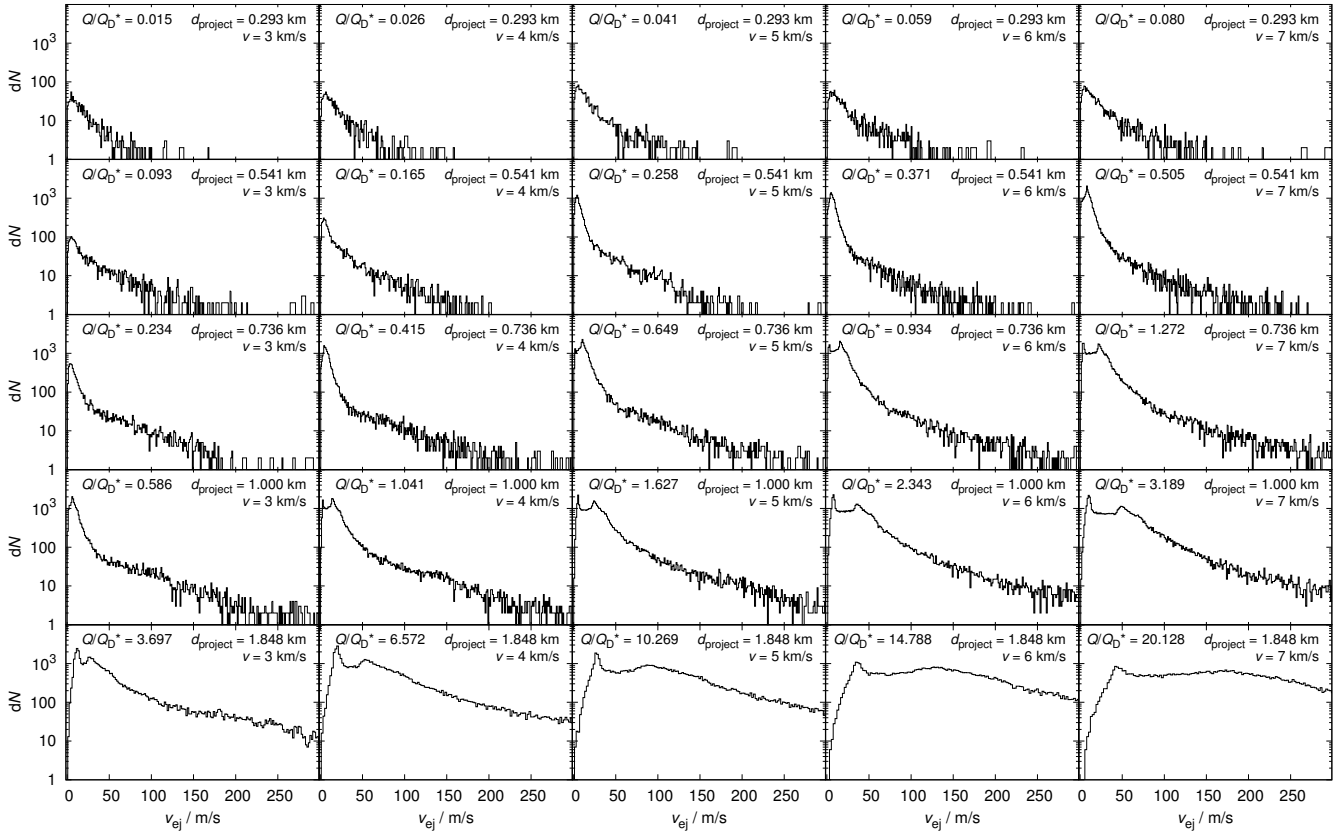

Figure B.11: Impact angle 30°

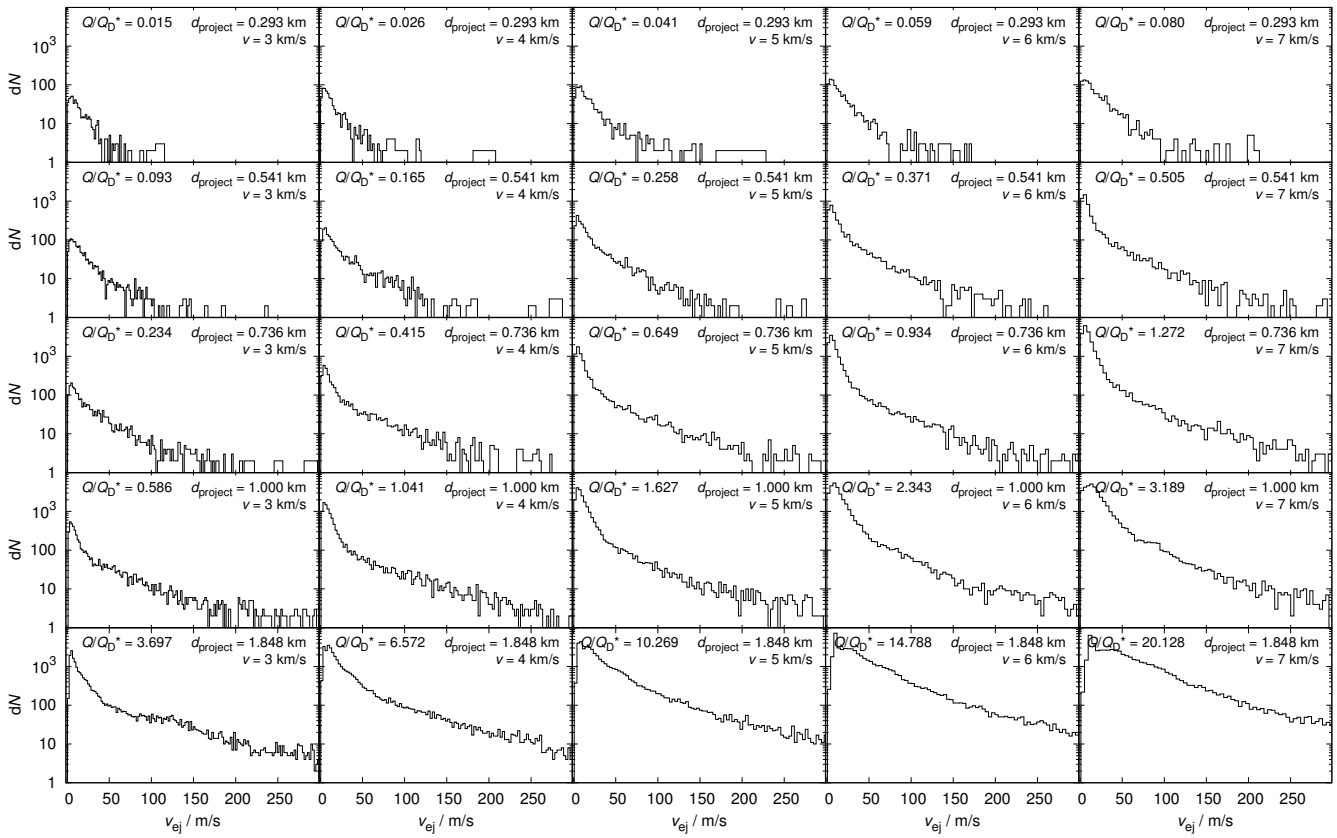

Figure B.12: Impact angle 60°

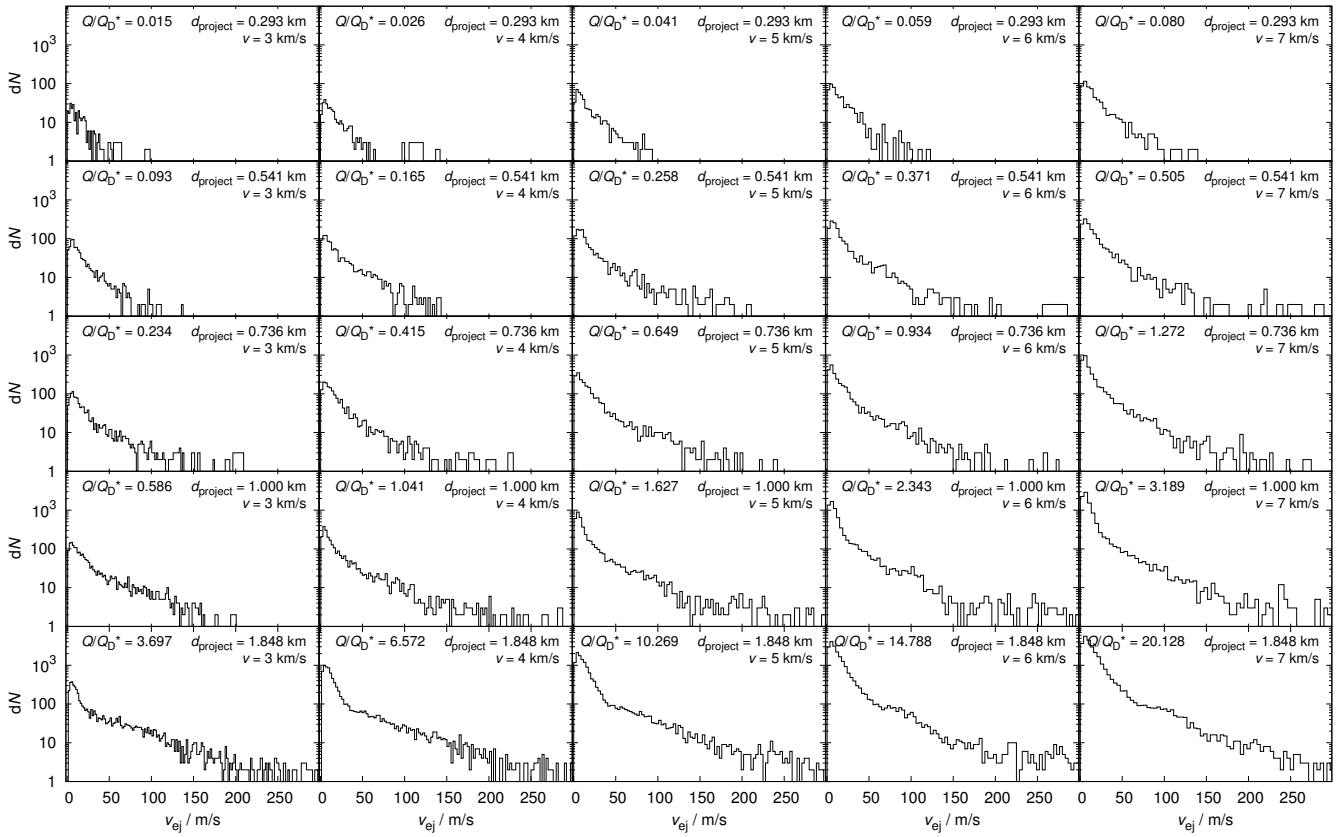

Figure B.13: Impact angle 75°

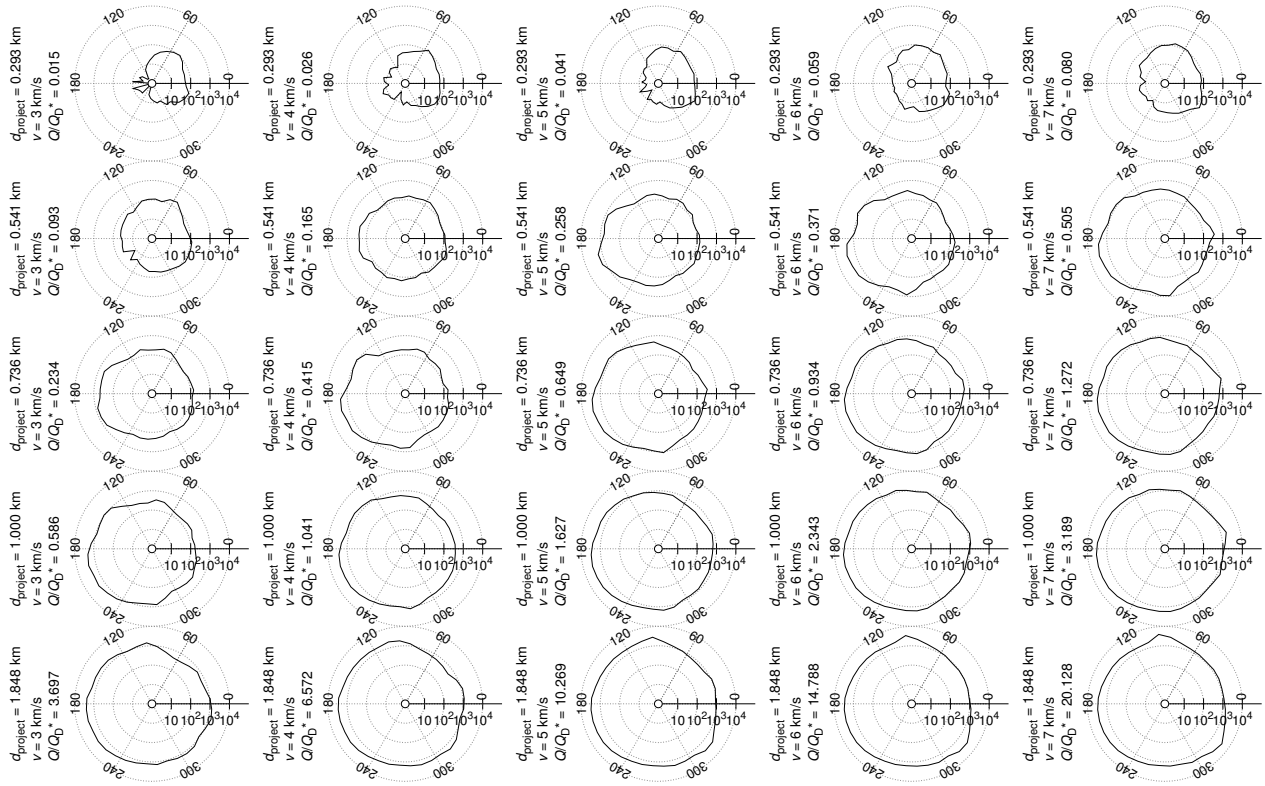

Figure B.14: Impact angle 15°.

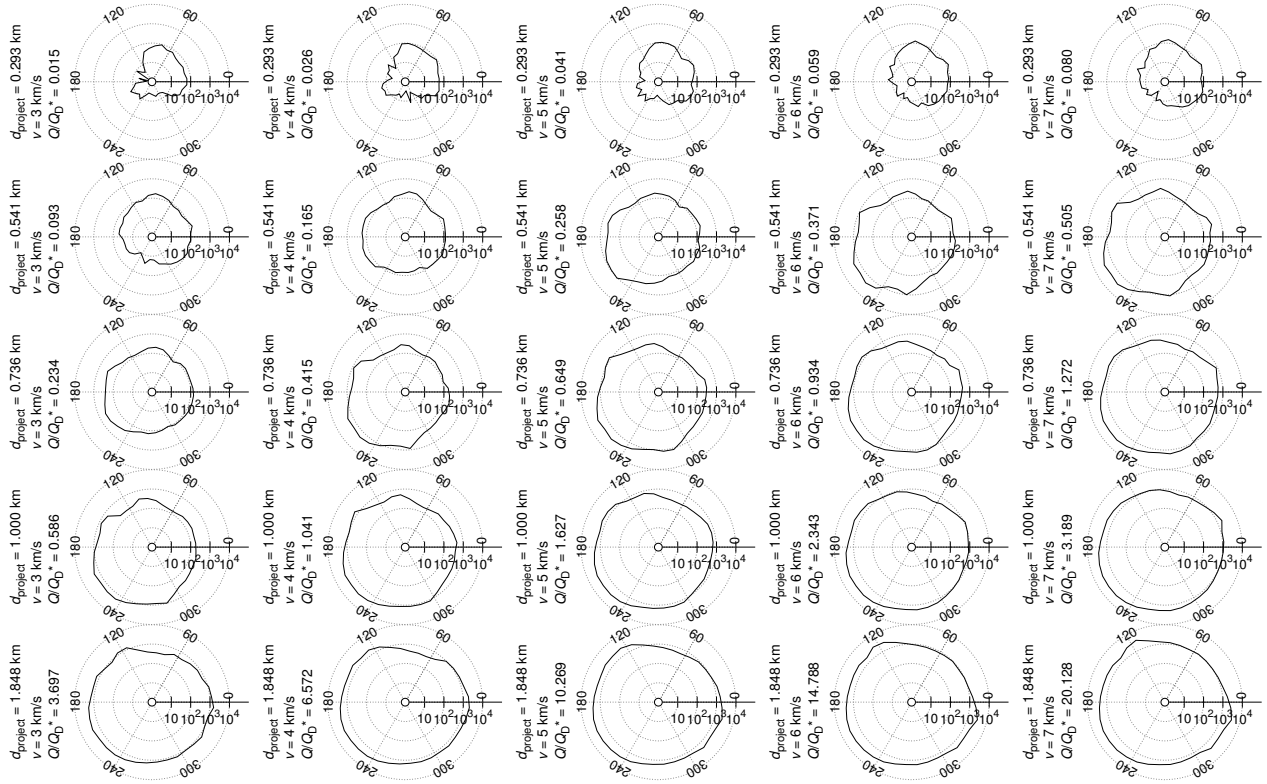

Figure B.15: Impact angle 30°.

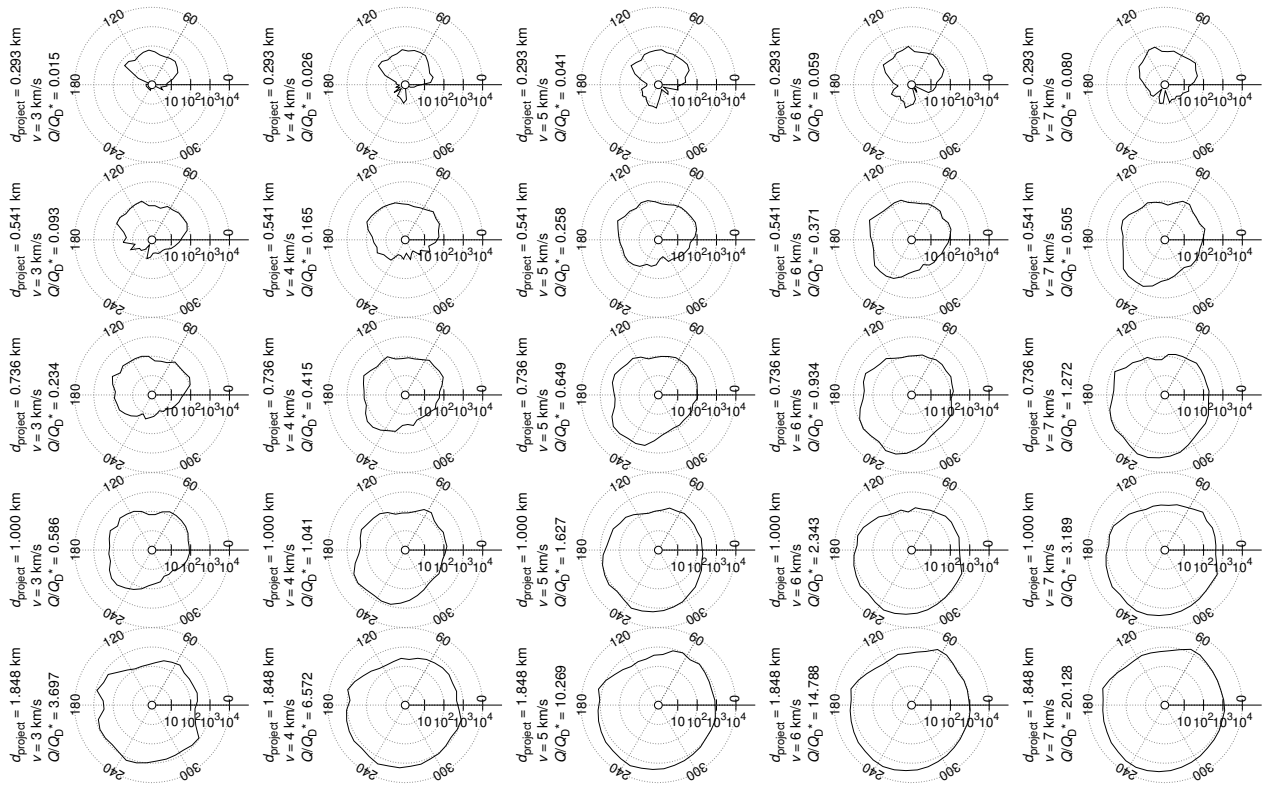

Figure B.16: Impact angle 60°.

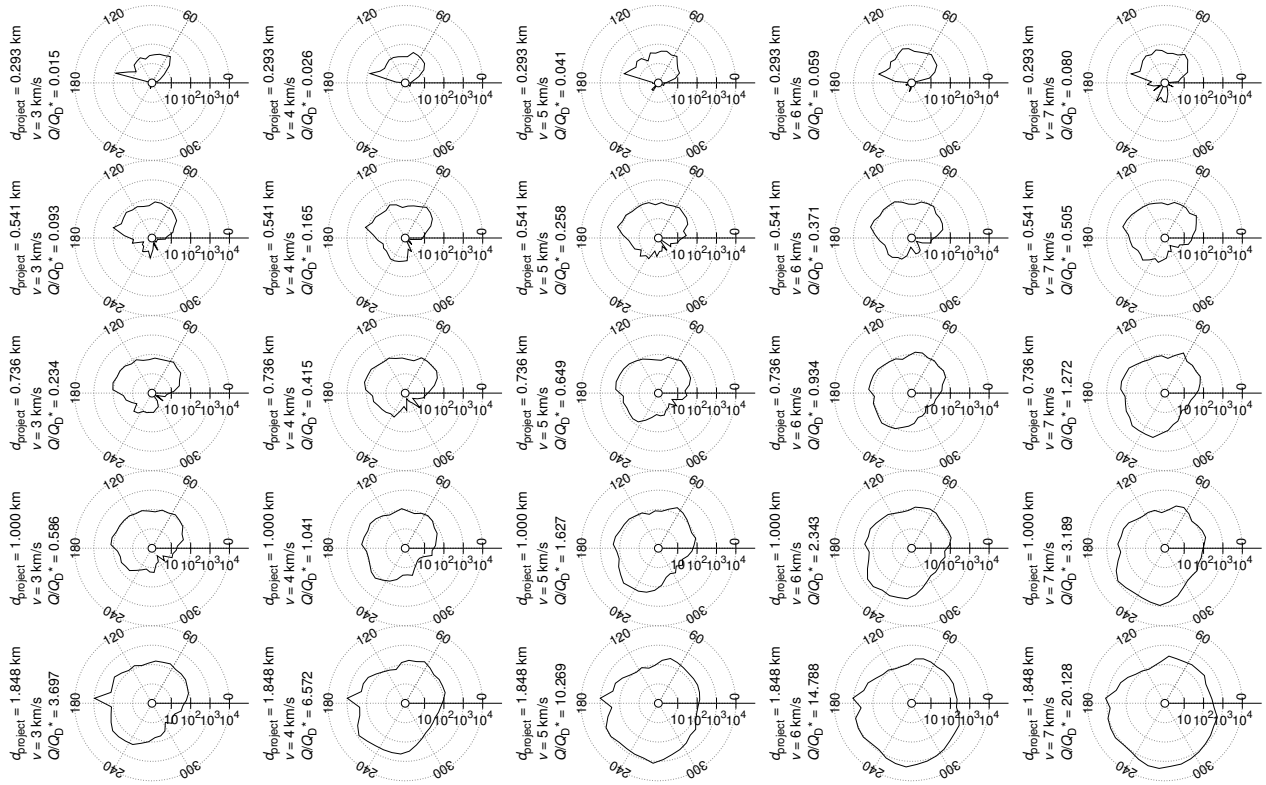

Figure B.17: Impact angle 75°.

Richardson, D. C., Quinn, T., Stadel, J., Lake, G., Jan. 2000. Direct Large-Scale N-Body Simulations of Planetesimal Dynamics. Icarus 143, 45–59.

Rosswog, S., Apr. 2009. Astrophysical smooth particle hydrodynamics. New A Rev.53, 78–104.

Rosswog, S., Apr. 2015. Boosting the accuracy of SPH techniques: Newtonian and special-relativistic tests. Mon. Not. R. Astron. Soc. 448, 3628–3664.

Tillotson, J. H., 1962. Metallic equations of state for hypervelocity impact. General Atomic Report.

von Mises, R., 1913. Mechanik der festen krper im plastisch- deformablen zustand. Nachrichten von der Gesellschaft der Wissenschaften zu Gttingen, Mathematisch-Physikalische Klasse 1913, 582–592.

Weibull, W., 1939. A Statistical Theory of the Strength of Materials. Ingeniörsvetenskapsakademiens handlingar. Generalstabens litografiska anstalts förlag.